applied sciences

Article

Microstructure and Fatigue Performance of Ti6Al4V Produced by Laser Powder Bed Fusion after Post-Heat Treatment

Yulong Yang [1,2,3,†], Meng Zhao [4,†], Hong Wang [1], Kai Zhou [1,2,3], Yangdong He [1], Yuyi Mao [5], Deqiao Xie [6], Fei Lv [1,7] and Lida Shen [1,*]

1 College of Mechanical and Electrical Engineering, Nanjing University of Aeronautics and Astronautics, Nanjing 210016, China
2 JITRI Institute of Precision Manufacturing, Nanjing 211806, China
3 Nanjing Hangpu Machinery Technology Co., Ltd., Nanjing 211806, China
4 FalconTech Co., Ltd., Wuxi 214028, China
5 National Center of Inspection on Additive Manufacturing Products Quality (JIANGSU), Wuxi 214028, China
6 College of Energy and Power Engineering, Nanjing University of Aeronautics and Astronautics, Nanjing 210016, China
7 Laboratory of High Power Fiber Laser Technology, Shanghai Institute of Optics and Fine Mechanics, The Chinese Academy of Sciences, Shanghai 201800, China
* Correspondence: ldshen@nuaa.edu.cn
† These authors contributed equally to this work.

Abstract: With the development of additive manufacturing (AM), the Ti-6Al-4V alloy manufactured by laser powder bed fusion (LPBF) is becoming more widely studied. Fatigue fracture is the main failure mode of such components. During LPBF processing, porosity defects are unavoidable, which hinders the exploration of the relationship between fatigue performance and microstructure. In this study, a laser remelting method was used to reduce porosity defects inside the Ti-6Al-4V alloy. Three annealing treatments (AT) and three solution-aging treatments (SAT) were used to study the effect of the two-phase zone ($\alpha + \beta$) microstructure on fatigue life and fatigue crack growth behavior. Fatigue life and crack growth rate (CGR) curves were obtained, and fatigue fracture surface and crack growth fracture surface were analyzed. The results show that microstructure influences fatigue life but has little effect on CGR. Compared with the as-built specimen, the fatigue life of the AT and SAT specimens increased significantly at 850°C by 101 and 63.7 times, respectively. The thickness of the α lath and the location of crack nucleation together affect the fatigue life. In the stable growth stage, the layered microstructure of α colonies is the most resistant to crack growth.

Keywords: laser powder bed fusion; heat treatment; Ti-6Al-4V; fatigue performance

check for updates

Citation: Yang, Y.; Zhao, M.; Wang, H.; Zhou, K.; He, Y.; Mao, Y.; Xie, D.; Lv, F.; Shen, L. Microstructure and Fatigue Performance of Ti6Al4V Produced by Laser Powder Bed Fusion after Post-Heat Treatment. *Appl. Sci.* **2023**, *13*, 1828. https://doi.org/10.3390/app13031828

Academic Editors: Michael Oluwatosin Bodunrin, Desmond Klenam, Japheth Obiko and Myoung-Gyu Lee

Received: 9 December 2022
Revised: 28 January 2023
Accepted: 30 January 2023
Published: 31 January 2023

1. Introduction

Ti-6Al-4V is commonly employed in the aerospace industry for its excellent specific strength and corrosion resistance [1–3]. It has become an indispensable structural material in aero engines, primarily used as compressor discs and blade casings to reduce engine mass and improve thrust ratio. In the processing of complex titanium alloy aerospace structural parts, traditional methods suffer from poor machinability, complicated processes, and expensive costs. However, LPBF has advantages in these aspects and has been widely used [4,5]. Reliability studies have become the focus of studies on the LPBF method.

LPBF melts and solidifies Ti-6Al-4V powder "point-by-point and layer-by-layer" with a high-energy laser [6]. During LPBF, the small laser melting pool and large temperature gradient lead to the generation of defects, thermal stress accumulation, and the formation of unbalanced phases [6]. These will affect mechanical properties and result in premature fatigue failure [7–9]. Research shows that fine needle martensite α' is the main phase of LPBF Ti-6Al-4V, while traditional forging or casting is dominated by equilibrium phases α

and β [10,11]. Therefore, the use of heat treatment to regulate the non-equilibrium phase is a necessary process after LPBF processing.

Aircraft engines are subjected to cyclical and complicated loads, so the material's properties must match the operating load requirements. Many things influence fatigue properties, including defects, rough surfaces, residual stress, and microstructure [7,12–16]. V. Chastand et al. [16,17] showed that defects such as gas porosity and lack of fusion (LOF) are the main reasons for the lower fatigue life of LPBF parts compared to traditional parts. Hanchen Yu et al. [7,18,19] evaluated the impact of surface finishing on the fatigue performance of LPBF Ti-6Al-4V, including turning, grinding, sandblasting, and polishing. It was discovered that reducing surface roughness significantly improved fatigue properties, with the polishing process having the best effect. Óscar T et al. [8,20] found that heat treatment has the potential to reduce residual stresses and improve fatigue life. Meng et al. [9,21,22] found that higher porosity (0.25–4%) makes it difficult to examine the effect of microstructure on fatigue performance due to excessive defects. The impact of microstructure on mechanical characteristics gradually becomes more apparent when defects are reduced.

The influence of microstructure on the fatigue performance of LPBF parts is often difficult to accurately determine due to the presence of defects, so it is necessary to reduce the number of defects. Numerous studies have shown that optimizing process parameters [13,19] and hot isostatic pressing (HIP) [15,16] can reduce porosity and thus improve fatigue performance. However, defects in LPBF parts cannot be completely eliminated. Currently, HIP is considered to be the most effective method to eliminate defects [15,16]. However, on the one hand, HIP will change the original microstructure, thus making the microstructure impossible to be effectively analyzed, while, on the other hand, the high cost also limits its application [7]. As an economical and feasible method, laser remelting can effectively reduce the porosity of parts and achieve ultra-low porosity (<0.01%) [21,23]. Remelting is critical in the reduction of porosity, and the underlying mechanism has been extensively studied and validated [23–25].

In summary, it is found that the current research on the fatigue performance of microstructures is very lacking and needs to be explored. In this study, a remelting strategy was used to reduce the influence of defects on fatigue properties by reducing the internal porosity of the formed specimens. Based on the heat treatment, the effect of microstructure in the two-phase zone on fatigue properties was analyzed in terms of fatigue life and fatigue expansion rate, and the patterns presented were investigated and summarized.

2. Materials and Methods

The parts were all produced by NCL-M150 additive manufacturing equipment (Nanjing Chamlion Laser Technology Co., Ltd., Nanjing, China). The gas atomization method was used to produce Ti-6Al-4V powder. Table 1 shows the powder's main chemical composition. Figure 1a displays the morphology and particle size distribution of the powder, which is between 10 μm and 90 μm, with an average of 42 μm. The parts were manufactured by remelting with the laser scanning speed and power tuned to 1800 mm/s and 160 W, respectively. The scanning strategy selected the serpentine path and 57°/67° rotation scanning. The remelted layer's scan path was perpendicular to the initial, and the laser scanning speed and power were adjusted to 1600mm/s and 180W, respectively. The diagram of the remelting operation is shown in Figure 1b, where the blue line was the initial scanning path and the red line was the remelting scanning path.

Table 1. Chemical composition of Ti-6Al-4V alloy powder (wt.%).

H	C	V	Al	Fe	O	Ti
0.0018	0.011	3.91	6.28	0.04	0.086	Bal.

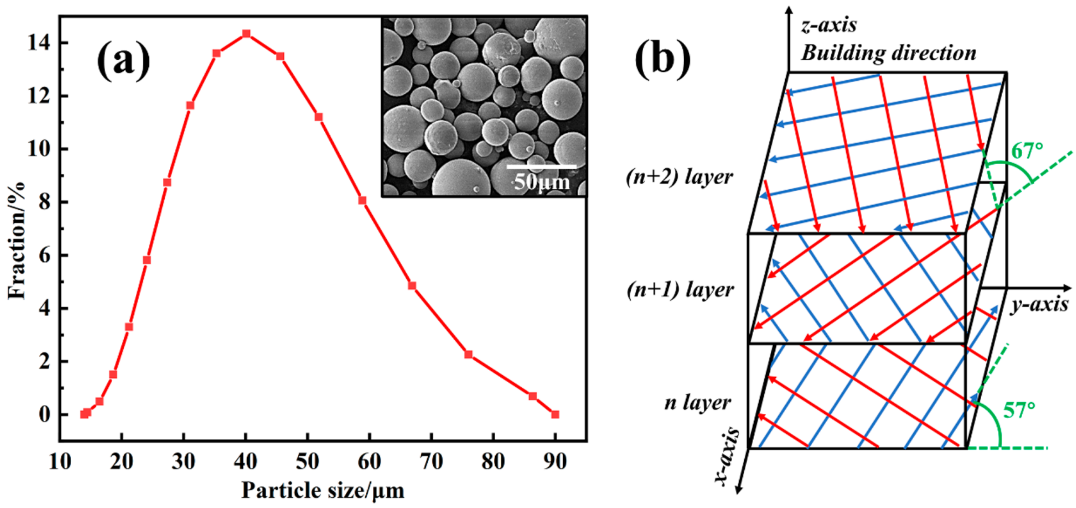

Figure 1. Morphology and particle size distribution of the powder (**a**) and schematic diagram of printing and scanning (**b**).

The remelting process can obtain nearly fully dense, high-quality Ti-6Al-4V specimens. Internal defects in LPBF parts are identified and counted using a 3D X-ray computed tomography (μ-CT) system. This approach ensures that these specimens have low and consistent porosity, thus guaranteeing the validity of microstructure analysis. Figure 2a,b are 3D defect diagrams of the fabricated specimens before and after the remelting process, respectively. The density of the specimen in Figure 2a is 99.762%, while in Figure 2b it is 99.998%. After remelting, the pores are greatly reduced, and the density is significantly improved.

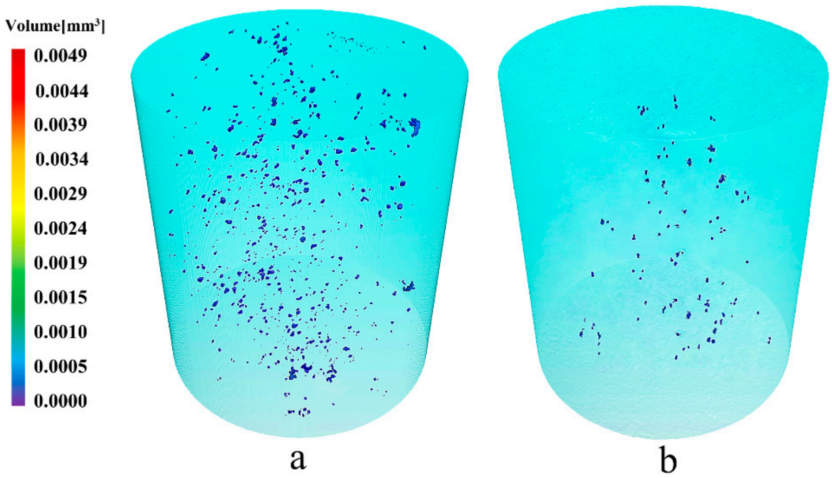

Figure 2. Three-dimensional pore diagram of the fabricated specimens before (**a**) and after (**b**) the remelting process.

The heat treatment was performed in a vertical tube furnace with a vacuum degree of greater than 10^{-6} MPa, and the temperature was increased at around 10 °C/min. The specific heat treatment protocols and markings are described in Table 2. Some of the fabricated specimens were used as the reference group, marked as "as-built"; others were subjected to AT and marked as 850FC, 950FC, and 1050FC, respectively; the remaining specimens were subjected to SAT, marked as 850WAC, 950WAC, and 1050WAC, respectively. In addition, scanning electron microscopy (SEM) and optical microscopy (OM) were used to examine the microstructure of Ti-6Al-4V.

Table 2. The specific heat treatment protocols and markings.

Specimen Marking	Heat Treatment Protocol
as-built	600 °C/2 h/FC
850FC	850 °C/2 h/FC
950FC	950 °C/2 h/FC
1050FC	1050 °C/2 h/FC
850WAC	850 °C/2 h/WC + 540 °C/4 h/AC
950WAC	950 °C/2 h/WC + 540 °C/4 h/AC
1050WAC	1050 °C/2 h/WC + 540 °C/4 h/AC

FC = furnace cooling; AC = air cooling; WC = water cooling.

Fatigue crack growth CT specimens and fatigue specimens were prepared according to the national standard specimen size, and the specific dimensions are shown in Figure 3. The initial length of prefabricated cracks in CT specimens is 2.6 mm. Before the test, specimens were polished and ground to reduce the influence of surface roughness on fatigue. The fatigue test at room temperature was carried out on the QBG-50 high-frequency fatigue testing machine.

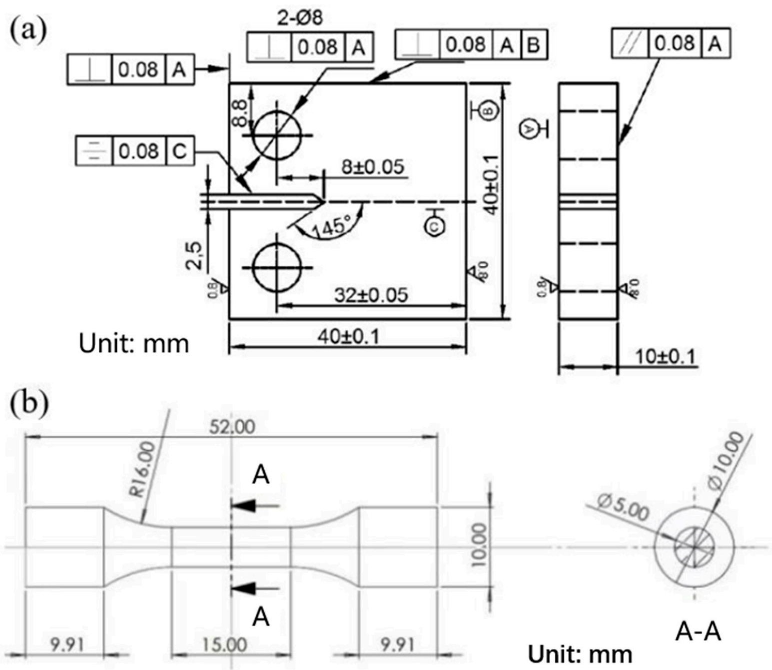

Figure 3. The dimensions of CT specimens (**a**) and fatigue specimens (**b**).

The fatigue test adopted uniaxial sinusoidal cyclic loading. The maximum stress (σ_{max}) was 500 MPa, the stress ratio (R) was −1, and the vibration frequency (f) was 110 Hz. This load is similar to the operating conditions of the turbine blades investigated. Three replicated tests were conducted and averaged. The room-temperature fatigue crack growth test was carried out using an Instron 8801 low-frequency fatigue testing machine. The test adopted cyclic sine wave loading, and the crack length was detected by the potential method, and σ_{max} was 2.5 kN, R was 0.1, and f was 10 Hz.

3. Results

3.1. Impact of the Heat Treatment on Microstructure

Numerous studies have discussed the mechanical performance and microstructure of as-built specimens in detail [11,14,18,26]. Therefore, they will be described briefly in this paper. This study uses six different heat treatment schedules to give Ti-6Al-4V a broad (α + β) microstructure. Figures 4 and 5 show their effects on the microstructure.

During the LPBF process, a complete acicular α′ martensite structure was formed, with equiaxed β grains of various sizes in the cross-section and long primary β columnar grains in the longitudinal section. Representative 3D microstructures of the 850FC and 950FC specimens are displayed in Figures 4a and 4b, respectively. The transformation point temperature (T_β) of Ti-6Al-4V is 995°C. Annealing below T_β doesn't alter the structural characteristics of the primary β columnar grains. Compared with 850FC, the heat treatment temperature (T_a) of 950FC is closer to T_β, resulting in a thickening of the α and β phases. The high magnification image in Figure 5a shows that the fine needle α-laths in 850FC have β phase structure outside the grain boundaries. The grain boundaries between α and β phases in Figure 5b are clearer. A similar microstructure was also found by Punit Kumar et al. [27] after heat treatment at temperatures below T_β. When 1050FC is heat treated at a temperature higher than T_β (Figure 4c), the complete β-phase microstructure formed an (α + β) layered structure during the slow cooling process. Since the size of equiaxed β grains limits the size of α colonies, at high temperatures, β grains grow rapidly and α colonies grow accordingly. Lütjering [28] showed that α colony size was a determinant of mechanical properties. From the above, temperature determines the final microstructure, and increasing temperature promotes the growth of a large number of grains. According to the Burgers relationship [29], the α phase grows preferentially parallel to the β phase crystallographic plane family. These planes grow relatively fast, and the α phase forms into plates and layers.

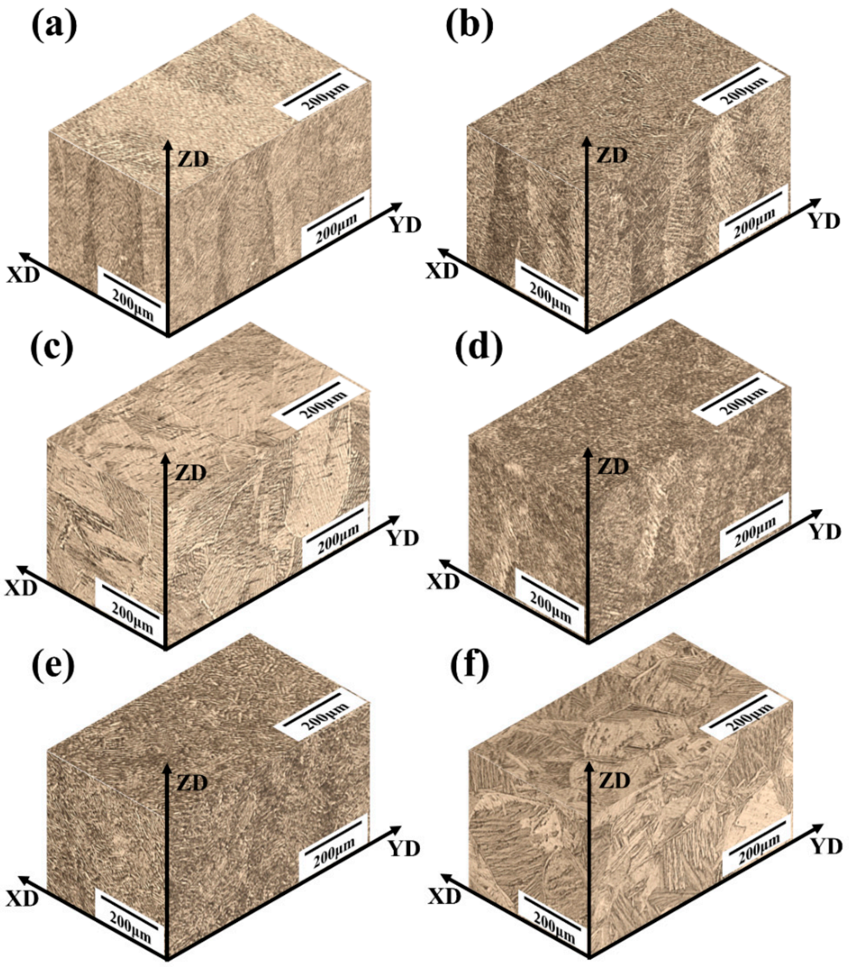

Figure 4. Representative 3D microstructures (OM) of Ti6Al4V following heat treatment schedules: (**a**) 850FC, (**b**) 950FC, (**c**) 1050FC, (**d**) 850WAC, (**e**) 950WAC, (**f**) 1050WAC.

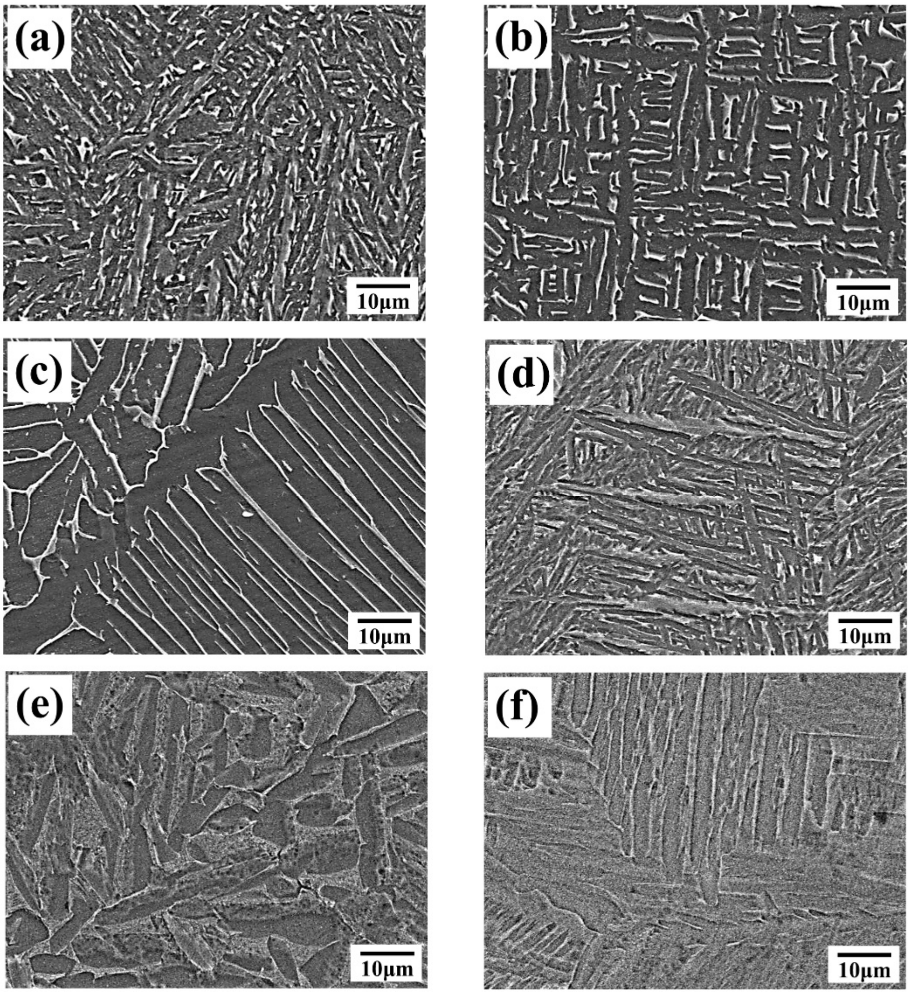

Figure 5. Representative microstructures (SEM) of Ti6Al4V specimens following heat treatment schedules (**a**) 850FC, (**b**) 950FC, (**c**) 1050FC, (**d**) 850WAC, (**e**) 950WAC, (**f**) 1050WAC.

The β phase in the two-phase zone is too late to undergo a diffusion-type transformation during the quenching process of SAT specimens, and a metastable martensite α′ phase is formed. Followed by the aging strengthening operation at 540 °C, the long holding time promotes the decomposition of acicular martensite α′, and the dissolved secondary α and β phases are dispersed around the primary α phase, resulting in a stable (α + β) structure. The formation mechanism of similar microstructures has also been confirmed in other studies [30]. Figure 4d,e display representative 3D microstructures of 850WAC and 950WAC, respectively. Compared with 850FC and 950FC, the needle-like α phase is coarsened and deformed. Part of the α phase in 950WAC has obvious spheroidization, which is due to the continuous growth of the primary α-phase in the aging process. Since the solution temperature of the 950WAC is closer to T_{β}, the grains grow and become coarser during the solution process. The unstable phase formed during quenching is decomposed during aging, and nucleation growth occurs subsequently. The primary α phase spheroidizes seriously, which further increases the inhomogeneity of the structure, which can also be clearly seen in Figure 5e. At the same time, the β phase cannot easily be observed under high magnification. This shows that the amount of precipitation is small. For 1050WAC, the aging process is carried out in the fully metastable α′ phase due to quenching above T_{β}. As illustrated in Figure 4f, the α colonies were clearly visible after aging and the equiaxed primary β grains in the cross-section were completely eliminated. Because of the different cooling methods, the average size of α colonies of the 1050FC specimen is smaller than that of 1050WAC. In Figure 5f, the α phase grows sufficiently, and the grain orientation in each α colony remains consistent.

For specimens with $T_a < T_\beta$, the precipitation mechanism of the β phase in the microstructure is different from $T_a > T_\beta$. When $T_a < T_\beta$, the metastable α′ phase turns into α phase by removing the V element from the transformation product, and the aggregation of the V element generated along the slatted α phase border causes the β phase to nucleate [31]. However, when $T_a > T_\beta$, the lath α nucleated at the primary β columnar grain boundaries grows rapidly towards the radial direction of the grain, which is displayed in Figure 5c,f. The difference in T_a also leads to the change in the β phase composition in the microstructure. The 950FC specimen will have a higher V concentration along the α laths than the 850FC specimen due to the higher temperature. Therefore, it has a higher equilibrium β phase concentration. This is also confirmed in the study by Punit Kumar et al. [27].

The width of the slatted α phase was measured by "ImageJ" software. The acicular martensite α′ in the microstructure of the as-built specimens is only 0.87 ± 0.24 μm. For Ta < Tβ, the lath thickness distribution is between 1.8 ± 0.24 μm for the 850FC specimen, between 2.3 ± 0.24 μm for the 950FC specimen, between 1.9 ± 0.18 μm for the 850WAC specimen, and between 3.5 ± 0.21 μm for the 950WAC specimen. This indicates that the lath thickens with increasing Ta. For Ta > Tβ, the mechanical performance of the specimens is determined by α colonies. The α colony size of the 1050FC specimen is 328 μm ± 10 μm, while that of the 1050WAC specimen is 198 ± 8 μm. This indicates that the colony size depends on the cooling rate and is negatively correlated.

3.2. Fatigue Performance of Heat Treatment

3.2.1. Average Fatigue Lifespan

Figure 6 shows the change in the average fatigue life (N) of different heat-treated specimens relative to the as-built specimens. All heat-treated specimens improve their fatigue performance at 500 MPa compared with as-built specimens. In Figure 6a, 850FC exhibits better fatigue life, which increased by 101 times compared with the finished specimens. In Figure 6b, the fatigue life change shows the same trend. 850WAC showed better fatigue life, which increased by 63.7 times. Other heat treatments also improved the fatigue life, but not significantly. As a result, the fatigue life of the specimens is improved because of microstructural changes, and the 850 °C specimens exhibit significantly better fatigue performance, which is something we need to focus on.

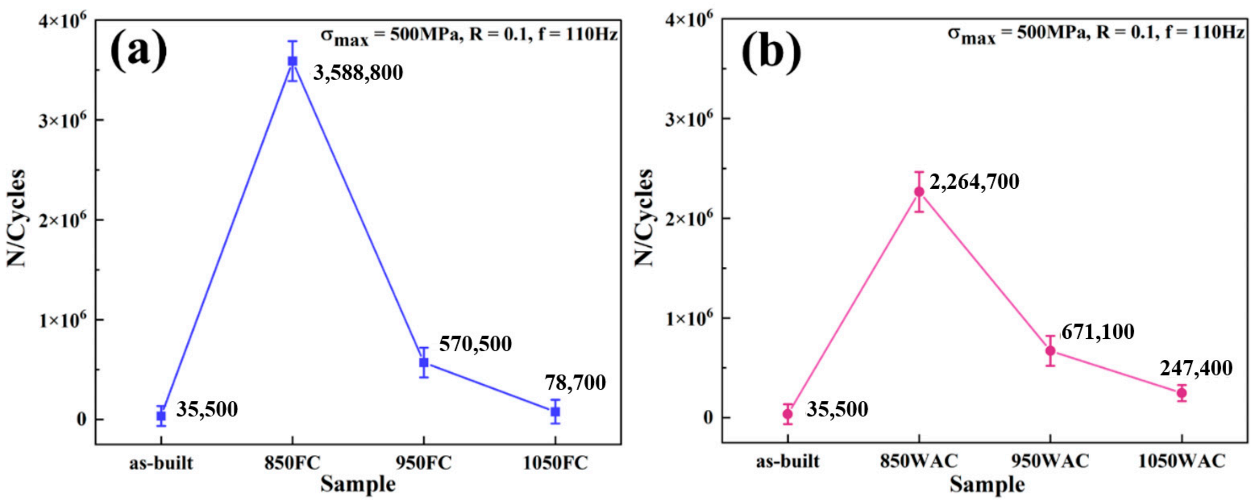

Figure 6. Average fatigue life(N) change curve of different heat-treated specimens: (**a**) AT, (**b**) SAT.

However, compared to wrought titanium alloys [32], the fatigue life of the LPBF specimens all show a significant loss, and the reason is the high sensitivity of the fatigue properties to defects. These defects are unavoidable in LPBF titanium alloys, and even with the remelting process, the residual tiny pores still have an effect on the fatigue properties.

3.2.2. Fracture Surfaces of Different Specimens

Figure 7 shows the representative fracture surface and crack initiation zone of the as-built specimen. The entire fracture surface is divided into three zones, as shown in Figure 7a. Among them, Zone I (the zone included in the red box) is the crack initiation zone. Figure 7b is an enlarged view of the crack initiation zone. Zone II is the crack propagation zone, which occupies most of the fracture surface area. Zone III is the transient interruption zone, which occurs when the load-bearing area is insufficient. Cracks occur in the polished as-built specimen at minor near-surface defects, which are LOF. The defect is located about 26 μm from the specimen's surface, and its fatigue life is 38,600 cycles. During fatigue propagation, the dominance of the multi-faceted fracture morphology can be seen, indicating the lower toughness of the as-built specimen. There are also many holes in the crack propagation surface near the transient fracture zone, indicating that the fatigue fracture is brittle and associated with the "brittleness" of the acicular martensite of the as-built specimen. The lower fatigue life also indicates that the acicular martensite structure has a low resistance to crack initiation—that is, the acicular martensite is more sensitive to porosity.

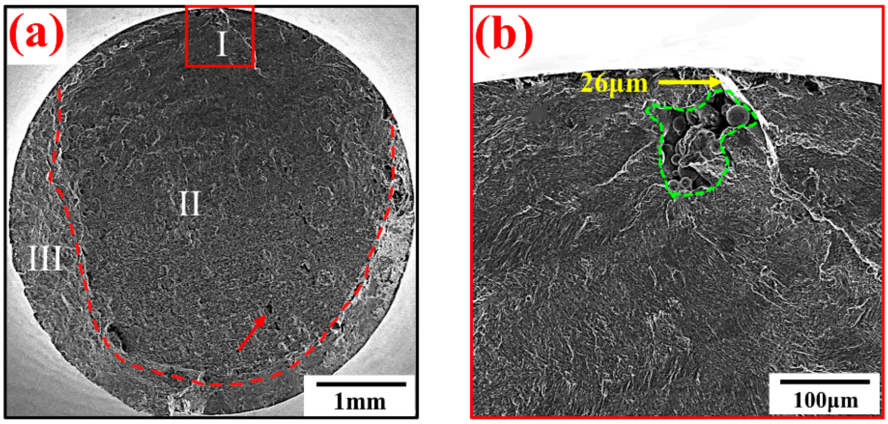

Figure 7. Macroscopic fatigue fracture surface (**a**) and the crack initiation zone (**b**) of the as-built specimen.

Figure 8 shows representative fracture surfaces of different heat-treated specimens. The figure indicates that each heat treatment fatigue specimen initiates cracks from the defects on or near the surface, and all propagate from a single source. The fracture surfaces are clearly divided into three zones. By comparison, it is found that the fatigue propagation surface (zone II) of 850FC and 950FC is relatively smooth (Figure 8a,b), 850WAC and 950WAC followed (Figure 8d,e), and 1050FC and 1050WAC (Figure 8c,f) exhibited a rougher surface. No obvious river lines can be seen on the smooth surface, meaning that it has good plasticity. On the contrary, the river pattern is obvious on the rough surface, which means brittleness, which is also consistent with the performance of the microstructure. The β phase in the two-phase zone improves the plasticity of the material, while with the coarsening of the α phase, the dislocation stress increases and the plasticity decreases, so 850FC shows a smoother surface. Comparing zone III, it is found that 1050FC and 1050WAC show a smaller area of the transient fracture area, indicating that the α colony exhibits better resistance to fatigue fracture.

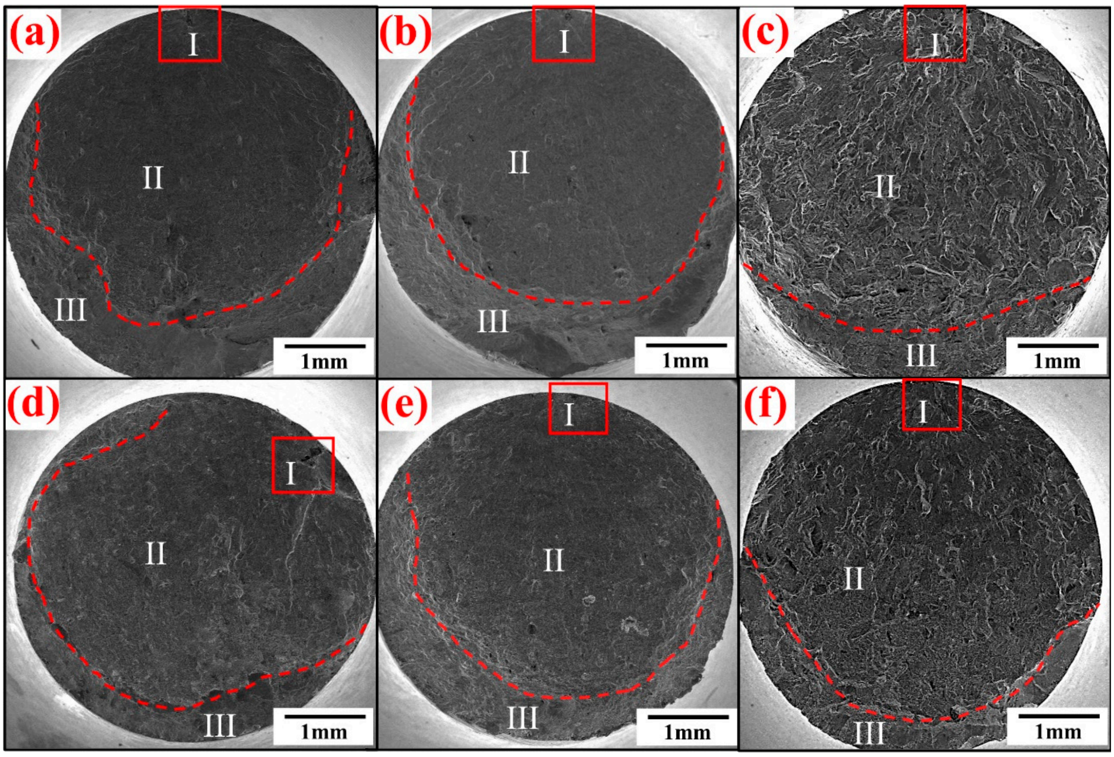

Figure 8. Macroscopic fatigue fracture surface of different specimens: (**a**) 850FC (2,733,000 cycles), (**b**) 950FC (575,400 cycles), (**c**) 1050FC (78,700 cycles), (**d**) 850WAC (1,521,300 cycles), (**e**) 950WAC (671,100 cycles), (**f**) 1050WAC (141,700 cycles).

Figure 9 shows the crack initiation zone of the heat-treated specimens corresponding to Figure 8. The figure indicates that all of the heat-treated specimens were fatigue fractured due to LOF defects near the surface, and the fatigue cracks propagated in a fan shape. The crack initiation of 850FC (Figure 9a) is about 15 μm from the specimen's surface, with a fatigue life of 2,733,000 cycles, showing a high fatigue life. The crack initiation of 950FC (Figure 9b) is about 3 μm from the specimen's surface, with a fatigue life of 575,400 cycles. The crack origin of 1050FC (Figure 9c) is about 8 μm away from the specimen's surface, with a fatigue life of 78,700 cycles. The surface of the source zone shows obvious cleavage morphology, and a large red arrow can be observed. The larger the grain size, the larger the cleavage plane, which also verifies that the macroscopic mechanical properties are determined by the size of α colony. 850WAC (Figure 9d) nucleated from relatively large surface defects, with a fatigue life of 1,521,300 cycles. Both 950WAC (Figure 9e) and 1050WAC (Figure 9f) nucleated from tiny pores on the surface, with a fatigue life of 671,100 and 141,700 cycles, respectively. The cleavage characteristics of the 1050WAC source zone are not obvious, and secondary cracks appear in the propagation zone (red arrow).

Comparing the fatigue life of each heat-treated specimen in Figure 9, in general, when the size of the pore defects at the origin of the crack is similar and the distance from the surface is similar, the impact of the microstructure on the fatigue life shows a certain law. As the width of the slatted α phase increases, the fatigue life of the specimen decreases, which is the same as the average fatigue life. Comparing 850FC and 850WAC, it can be found that when the grain size is not much different, the larger the LOF defect, the lower the fatigue life. In the heat treatment study of traditional titanium alloys [33], for the layered microstructure, the high cycle fatigue life can be controlled by the layer width or the grain size. This is compatible with the experimental results of this study.

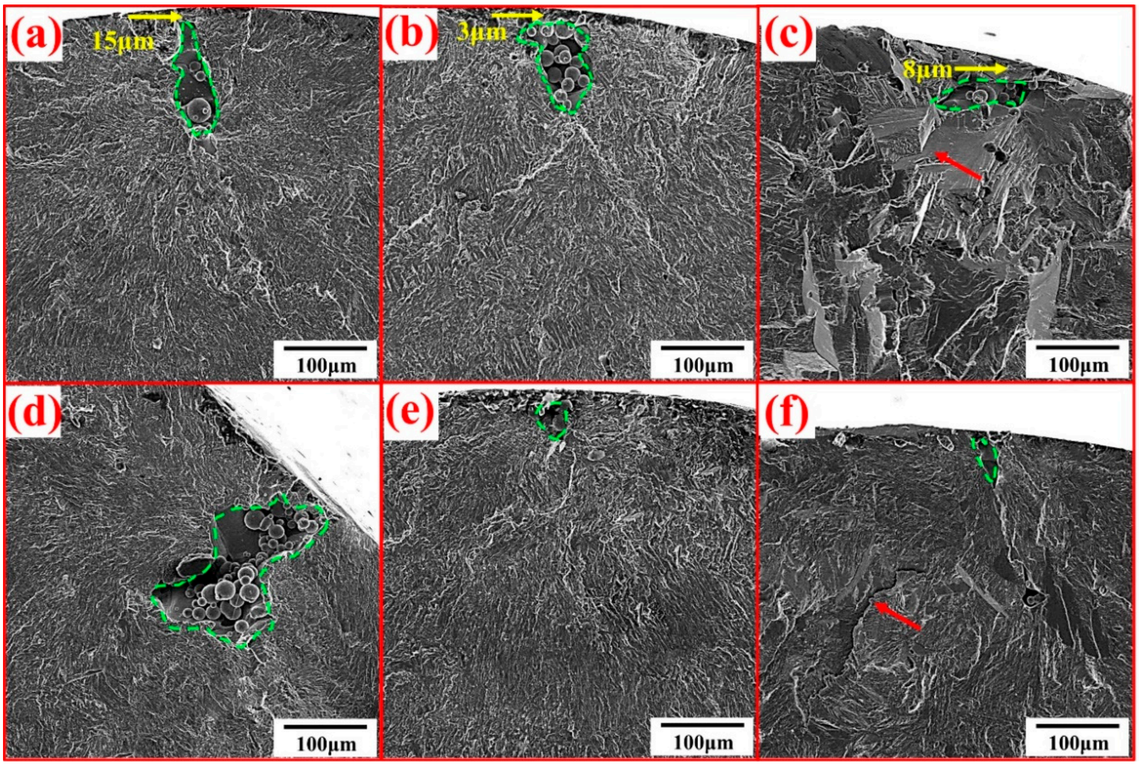

Figure 9. Macroscopic crack initiation zone of different specimens: (**a**) 850FC (2,733,000 cycles), (**b**) 950FC (575400 cycles), (**c**) 1050FC (78,700 cycles), (**d**) 850WAC (1,521,300 cycles), (**e**) 950WAC (671,100 cycles), (**f**) 1050WAC (141,700 cycles).

Figure 10 shows another representative fracture surface and crack initiation zone of 850FC and 850WAC, respectively. The crack initiation zone I moves inward, and the fatigue fracture nucleates from the internal defects that are far from the surface, as displayed in Figure 10a,c. The enlarged view of the crack initiation zone of 850FC is displayed in Figure 10b. The defect is located about 658 μm from the surface, and its fatigue life is 3,961,000 cycles. Compared with 850FC in Figure 9a, the site of crack initiation also caused a further improvement in fatigue life, indicating that the location of crack initiation and the microstructure jointly caused the improvement in fatigue life. Figure 10d shows an enlarged diagram of the crack initiation of 850WAC, the depth of the defect from the surface is about 118 μm, and the fatigue life is 2,175,400 cycles. The fatigue life is significantly improved compared to 850WAC in Figure 9d. The experimental results indicate that the deeper the crack initiation location, the longer the fatigue life. The microstructure and initiation location jointly determine the fatigue life.

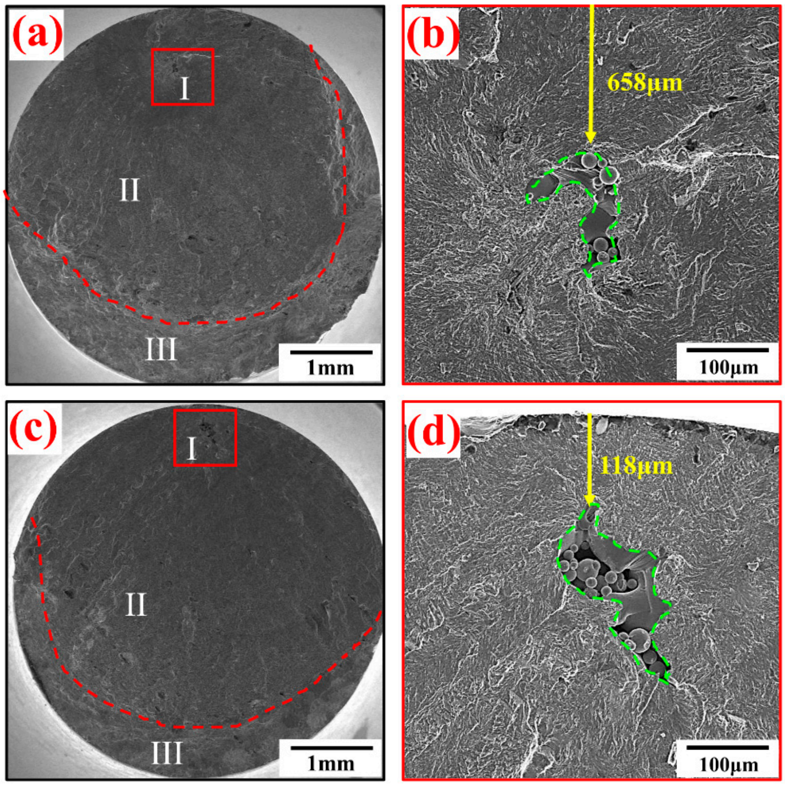

Figure 10. Macroscopic fatigue fracture surface and the crack initiation zone of different specimens: (**a**,**b**) 850FC (3,961,000 cycles), (**c**,**d**) 1050WAC (2,175,400 cycles).

3.3. Effect of the Heat Treatment on Crack Growth Behaviour

3.3.1. Fatigue Crack Growth Rate

The fatigue crack growth rates (CGR) of identical-size CT specimens subjected to three different heat treatment processes were measured. The seven-point incremental polynomial method in ASTM E647 was used to calculate CGR curves in the linear Paris zone (zone II).

Figure 11a shows the CGR curves of the AT specimens obtained by the incremental polynomial method. In the AT specimens, different heat treatment temperatures show the same trend. When the stress intensity factor $\Delta k < 20$ MPa $m^{0.5}$, the CGR curve of 1050FC is the lowest while 950FC is the highest, but it is not much different from that of 850FC. When 20 MPa $m^{0.5} < \Delta k < 30$ MPa $m^{0.5}$, the difference between the CGR curves of all heat-treated specimens gradually becomes smaller, and the CGR of the as-built specimen remains similar to those of the heat-treated specimens. When Δk continues to increase, the CGR of the as-built specimens is higher than that of the heat-treated specimens. In the low Δk area, there is a certain fluctuation in the CGR. Overall, 1050FC has higher crack growth resistance, and the as-built specimen has the lowest.

Figure 11b shows the CGR curve of SAT specimens obtained by the incremental polynomial method. Compared with the AT specimens, the difference in CGRs of the SAT specimens is more obvious. When $\Delta k < 20$ MPa $m^{0.5}$, the CGR curve of 1050WAC is the lowest, followed by 950WAC. And 850WAC has the highest CGR. When 20 MPa $m^{0.5}$ < $\Delta k < 30$ MPa $m^{0.5}$, the difference between 850WAC and 950WAC gradually decreases, and the CGR curve of the constructed specimen remains similar to that of 850WAC. When Δk continues to increase, the CGR of the as-built specimen is higher than that of the heat-treated specimens, and the CGR of 1050WAC is gradually higher than 950WAC. Overall, 1050WAC has higher crack growth resistance, and the as-built specimen has the lowest crack growth resistance.

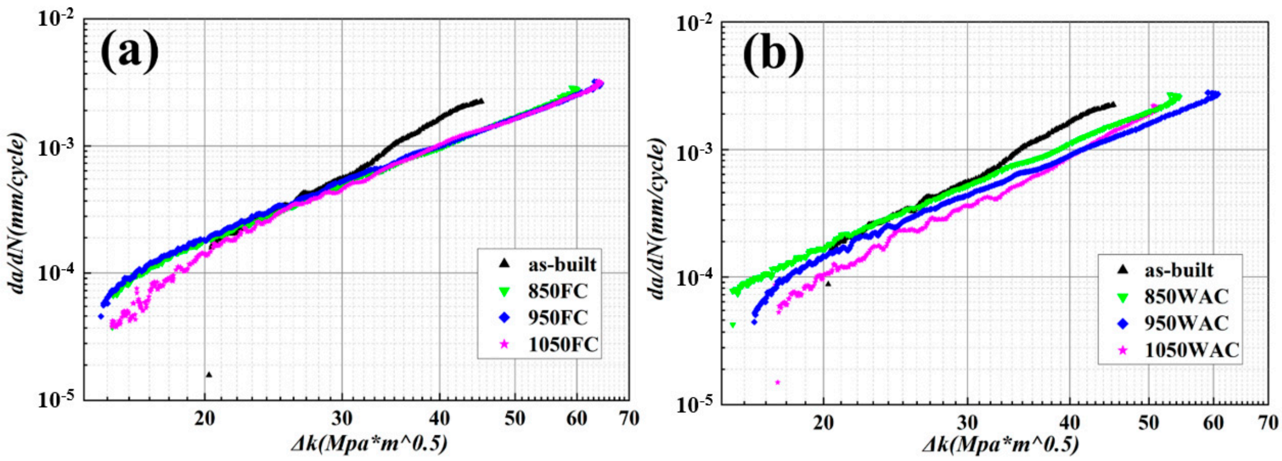

Figure 11. Comparison of CGR curves on different AT specimens: (**a**) and AST specimens: (**b**).

The linear zone (Zone II) satisfies the Paris equation:

$$da/dN = C(\Delta k)^m \tag{1}$$

The parameter m represents the slope of the scatter plot, and C and m comprehensively represent the value of the CGR. We fitted the CGR curves and calculated the parameters C and m, which are listed in Table 3. By comparison, it is found that in the Paris zone (zone II), 1050FC and 1050WAC have excellent resistance to fatigue crack growth. When $T_a < T_\beta$, the impact of the microstructure's change on the CGR is not obvious. When $T_a > T_\beta$, the presence of the large α colony can greatly improve the fatigue crack resistance of the specimens. large colony significantly increases the fatigue crack resistance of the specimens.

Table 3. Paris constants for different Specimens.

Specimen	C (Standard Error)	m (Standard Error)
850FC	7.6899×10^{-8}	2.56492
950FC	9.7163×10^{-8}	2.50276
1050FC	2.1053×10^{-8}	2.50923
850WAC	3.3787×10^{-8}	2.82557
950WAC	3.5072×10^{-8}	2.75541
1050WAC	6.3276×10^{-9}	2.81959

3.3.2. Fracture Surfaces of Different Specimens on Paris Zone

Figure 12 shows the fracture morphologies of the Paris zone of the fatigue crack growth specimens with different heat treatments. Fatigue cracks propagate from left to right, and it can be found that secondary cracks or micro-cracks appear on the fracture surfaces of all specimens. The fracture is dominated by cleavage fracture, and the width of the cleavage step gradually widens with the growth of α grains. On the plane of the partially cleaved steps, there are mutually parallel fatigue striations perpendicular to the nominal crack propagation plane, but not all steps. Fine fatigue striations appear on the cleavage facets of 850FC (Figure 12a) and 850WAC (Figure 12d), which are difficult to observe, and related to the fineness of α grains. The cleavage planes of 950FC (Figure 12b) and 950WAC (Figure 12e) are widened, and fatigue striations are also more obvious. The cleavage steps of 1050FC (Figure 12c) and 105WAC (Figure 12f) were further enlarged, and the secondary crack between the planes grows deeper into the material.

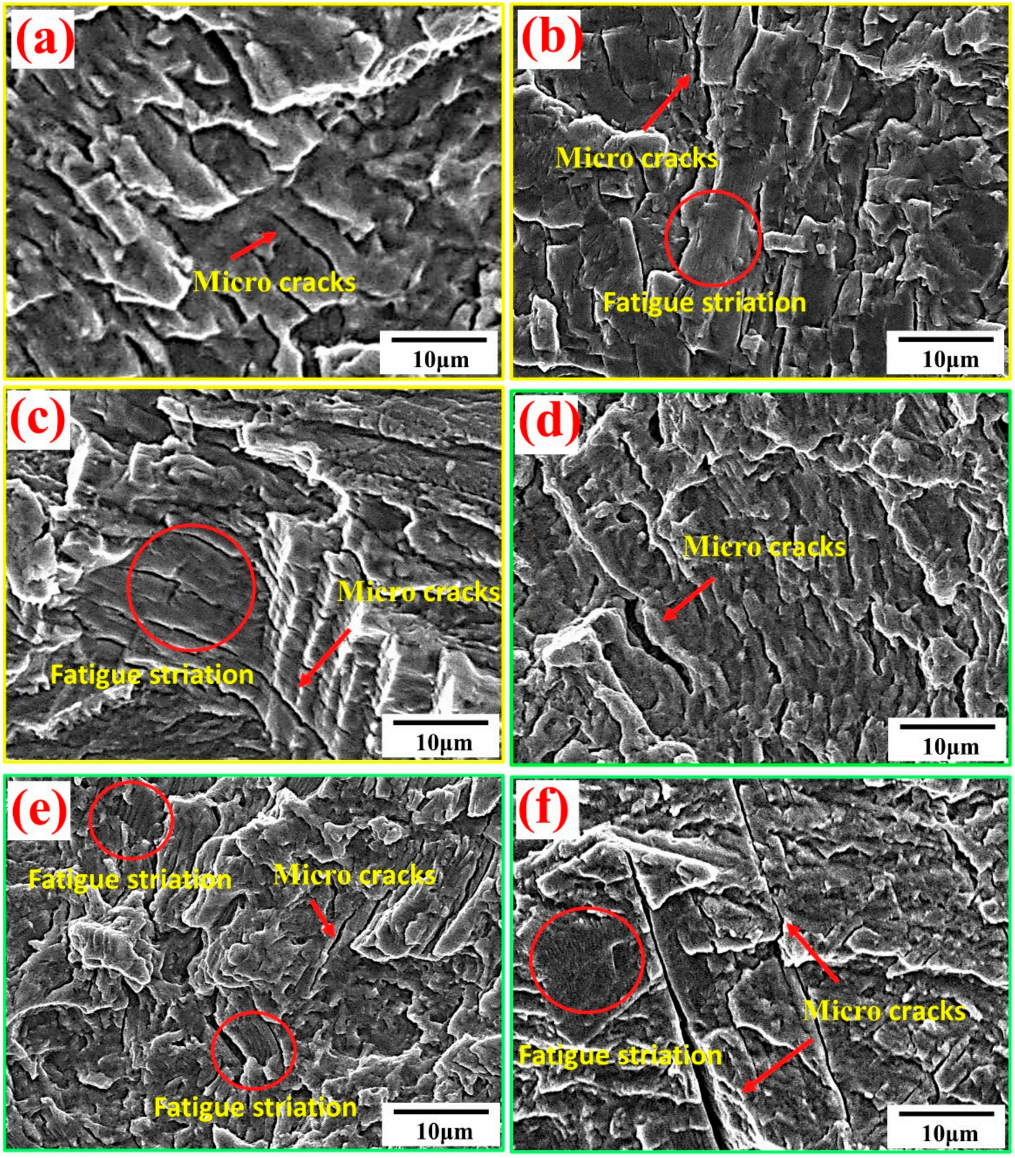

Figure 12. Fracture surfaces of different specimens on Paris zone: (**a**) 850FC, (**b**) 950FC, (**c**) 1050FC, (**d**) 850WAC, (**e**) 950WAC, (**f**) 1050WAC.

4. Discussion

4.1. Small Crack Growth

The fatigue life of the specimen is mainly made up of the crack initiation and propagation life. Specimen 1050FC (Figure 9c) has the lowest CGR and overall fatigue life performance in the crack growth stage, which is not significantly different from the as-built specimen. This indicates that the crack initiation stage occupies most of the entire life stage. The fatigue crack initiation stage is mainly determined by the irreversibility of slip [34]. In local grains with good sliding directions, dislocations nucleate and slide. Plastic strain builds up with cycle loading until it becomes incompatible with adjacent grain sliding. As a result, little extrusions and protrusions occur, finally forming a small crack, and the local sliding deforms the surface grains, which are likewise susceptible to these protrusions and extrusions. Therefore, cracks tend to nucleate from surfaces or defects and the stress concentration of the applied load tends to accelerate the formation of small cracks. Favorable microstructures tend to reduce dislocation motion and resist crack initiation.

The fatigue initiation life includes the small crack stage, and the length of the crack propagation is usually only a few hundred microns. At this time, the stress intensity factor is very small, and a favorable structure can significantly improve the crack initiation life at this stage [35,36]. After the initiation of a small crack, under the action of continuous cyclic loading, the small crack continues to propagate forward through slippage. The slip length determines microcracks' propagation [37]. For $T_a < T_\beta$, cracks tend to choose the most favorable direction for propagation to extend. Because grain boundaries are limited, the majority of small cracks propagate between them, and the crack propagation is zigzag. The secondary crack can share the stress at the tip of the main crack, and consume a lot of energy. This organizes further crack growth and extends the crack initiation life. Therefore, the smaller the α grains, the denser the grain boundaries. Slipping becomes more difficult as the dislocations accumulate at grain boundaries. This improves crack propagation resistance while also extending crack initiation life. For $T_a > T_\beta$, the small crack's propagation path tends to extend along the α colony boundary. When encountering another α colony boundary, dislocations accumulate at the α colony boundary and change the direction of expansion after accumulation to a certain extent. The size of the α colony reflects the length of the slip to some extent. The larger the colony, the longer the slip length after each deflection, the faster the crack propagation rate, and the worse the resistance to crack initiation.

4.2. Effects of Nucleus Position and Microstructure on Fatigue

During the experiment, only the fine ($\alpha + \beta$) two-phase microstructure appeared at the pore defects far away from the surface. Disregarding randomness, it is believed that a favorable microstructure increases the stress sensitivity of internal pores. Once the fatigue fracture is initiated from the inside, there will be river lines around the fatigue source, indicating that once the crack is initiated, it will spread around. It is confirmed that the crack will propagate along the plane perpendicular to the load at the stage of just beginning to propagate. This is congruent with the findings of Romali Biswal et al. [38]. After a certain position of the irregular pore defect becomes the crack initiation point, small crack propagation begins to occur. At this time, the area where the small crack propagation occurs yields, and the crack tip undergoes plastic deformation, while other parts around the pore defect are still below the elasticity threshold. With the loading of the cyclic load, the maximum stress concentration is gradually transferred to the surrounding elastic zone of the vertical loading axis, that is, one circle of the pores, so that the life of the small crack stage will be significantly improved. Therefore, in the case of low overall porosity, the favorable microstructure and the position of the pore defect will jointly control the fatigue life of the specimen after the defect near the interior becomes the crack source. According to the actual analysis results, a microstructure with as small a phase size as possible and fatigue originating from internal locations will achieve higher fatigue life.

4.3. Fatigue Crack Growth Rate Analysis

The range of stress intensity factors further increases as the crack enters the stable propagation stage (Paris zone). The growth rate of cracks at the early stage of stable propagation is mainly controlled by the thickness of the α lath [39]. For the as-built specimen, due to the thin thickness of the acicular martensite in the microstructure, when the crack tip encounters the acicular martensite, the dislocations accumulate at its boundary and eventually propagate through the martensite forward. After heat treatment, for $T_a < T_\beta$, after the crack encounters a thicker α slab, the crack penetration requires more energy, so the crack propagation direction changes. The major cause of the reduction in CGR is the deflection of the crack. For $T_a > T_\beta$, the α colony will complicate the crack propagation path, and differently oriented α colonies increase resistance to fatigue propagation. The excellent fatigue resistance of α colony microstructure is often related to the high deflection and bifurcation during crack propagation. The secondary crack caused by bifurcation will greatly share the stress intensity of the main crack tip and reduce the propagation rate.

As the crack length increases, the inhibitory effect of the microstructure is negligible, the plastic zone at the crack tip passes directly through multiple grains, and crack propagation begins to proceed along two slip systems or multiple slip systems simultaneously or alternately. When the crack propagates in this state, the load promoting crack growth varies with time, so the CGR also varies with time and stress intensity factor. The continuous plastic deformation and the fracture process affect the crack tip geometry, which in turn affects the fracture topography characteristics caused by crack propagation. The fatigue crack growth mechanism at this stage propagates in a plastic banding mechanism, and each cyclic loading of tensile loading will produce a fatigue band. The CGR is the lowest when the fatigue crack propagates in a plastic banding mechanism, which also explains why brittleness causes an increase in the fatigue fracture growth rate of the as-built specimen.

5. Conclusions

In this study, the effect of (α + β) two-phase microstructure on the fatigue life and fatigue crack growth properties of LPBF Ti-6Al-4V was investigated based on porosity reduction by remelting. The microstructure and morphology, average fatigue life, and CGR curves were obtained, and the fracture surfaces of fatigue specimens and fatigue crack growth specimens of different heat treatment processes were researched. The following are the main conclusions:

(1). The fatigue life changes of AT and SAT specimens follow the same pattern as heat treatment temperature increases. Heat treatment temperature rises, causing the slatted α phases to thicken and fatigue performance to deteriorate. The fatigue life of AT and SAT specimens at 850 °C increased significantly, by 101 times and 63.7 times, over the as-built specimen, respectively.

(2). By observing the fracture surfaces of fatigue specimens, it was found that the tiny defects inside the part still affected the location of the crack origin. The location of the crack nucleation and the microstructure together control the fatigue life of the fatigue specimen. The farther the nucleus position is from the surface, the higher the fatigue life.

(3). In terms of Paris CGR, when $T_a < T_\beta$, AT and SAT specimens both show less sensitivity to microstructure; When $T_a > T_\beta$, the α colony makes the CGR show excellent performance, which is due to the high deflection of the crack growth and the generation of secondary cracks.

(4). In the fracture faces of fatigue growth specimens, it was found that all heat-treated specimens were mainly cleavage fractures. Typical fatigue striation features appear on the cleavage steps, and secondary cracks are distributed between the steps. When $T_a > T_\beta$, the cleavage step is further widened and the secondary crack deepens.

(5). Regardless of whether it is AT or SAT, when $T_a < T_\beta$, the microstructure is composed of plate-like α and β phases. T_a determines the thickness of the α lath. The higher the T_a, the thicker the α lath. When $T_a > T_\beta$, the microstructure appears as α colonies. The size of α colonies depends on the cooling rate. The faster the cooling rate, the smaller the α colonies.

Author Contributions: Y.Y. and M.Z.: conceptualization, methodology, investigation, formal analysis, writing—original draft; K.Z. and D.X.: methodology, validation, writing—review and editing; H.W., Y.Y. and Y.H.: resources; D.X. and F.L.: formal analysis, writing—review and editing; L.S. and Y.M.: supervision, funding acquisition, writing—review and editing. All authors have read and agreed to the published version of the manuscript.

Funding: This work was supported by the National Natural Science Foundation of China (No. 51475238), the Key Research and Development Program of Jiangsu Provincial Department of Science and Technology of China (No. BE2019002), the China Post Doctoral Fund (No. 2020M671475).

Institutional Review Board Statement: Not applicable.

Informed Consent Statement: Not applicable.

Data Availability Statement: Data available on request due to restrictions eg privacy or ethical. The data presented in this study are available on request from the corresponding author. The data are not publicly available due to confidentiality.

Acknowledgments: We would like to express our appreciation to Jiangsu 3D Intelligent Manufacturing Research Institute for supporting this research.

Conflicts of Interest: The authors declare no conflict of interest.

References

1. Baudana, G.; Biamino, S.; Ugues, D.; Lombardi, M.; Fino, P.; Pavese, M.; Badini, C. Titanium aluminides for aerospace and automotive applications processed by Electron Beam Melting: Contribution of Politecnico di Torino. *Met. Powder Rep.* **2016**, *71*, 193–199. [CrossRef]
2. Zhang, X.; Chen, Y.; Hu, J. Recent advances in the development of aerospace materials. *Prog. Aerosp. Sci.* **2018**, *97*, 22–34. [CrossRef]
3. Hao, Y.-L.; Li, S.-J.; Yang, R. Biomedical titanium alloys and their additive manufacturing. *Rare Met.* **2016**, *35*, 661–671. [CrossRef]
4. Hamidi, M.; Harun, W.S.W.; Samykano, M.; Ghani, S.A.C.; Ghazalli, Z.; Ahmad, F.; Sulong, A.B. A review of biocompatible metal injection moulding process parameters for biomedical applications. *Mater. Sci. Eng. C Mater. Biol. Appl.* **2017**, *78*, 1263–1276. [CrossRef]
5. Liu, Y.J.; Ren, D.C.; Li, S.J.; Wang, H.; Zhang, L.C.; Sercombe, T.B. Enhanced fatigue characteristics of a topology-optimized porous titanium structure produced by selective laser melting. *Addit. Manuf.* **2020**, *32*, 101060. [CrossRef]
6. Lv, F.; Liang, H.; Xie, D.; Mao, Y.; Wang, C.; Shen, L.; Tian, Z. On the role of laser in situ re-melting into pore elimination of Ti–6Al–4V components fabricated by selective laser melting. *J. Alloys Compd.* **2021**, *854*, 156866. [CrossRef]
7. Yu, H.; Li, F.; Wang, Z.; Zeng, X. Fatigue performances of selective laser melted Ti-6Al-4V alloy: Influence of surface finishing, hot isostatic pressing and heat treatments. *Int. J. Fatigue* **2019**, *120*, 175–183. [CrossRef]
8. Shipley, H.; McDonnell, D.; Culleton, M.; Coull, R.; Lupoi, R.; O'Donnell, G.; Trimble, D. Optimisation of process parameters to address fundamental challenges during selective laser melting of Ti-6Al-4V: A review. *Int. J. Mach. Tools Manuf.* **2018**, *128*, 1–20. [CrossRef]
9. Singla, A.K.; Banerjee, M.; Sharma, A.; Singh, J.; Bansal, A.; Gupta, M.K.; Khanna, N.; Shahi, A.S.; Goyal, D.K. Selective laser melting of Ti6Al4V alloy: Process parameters, defects and post-treatments. *J. Manuf. Process.* **2021**, *64*, 161–187. [CrossRef]
10. Yang, L.; Zhicong, P.; Ming, L.; Yonggang, W.; Di, W.; Changhui, S.; Shuxin, L. Investigation into the dynamic mechanical properties of selective laser melted Ti-6Al-4V alloy at high strain rate tensile loading. *Mater. Sci. Eng. A* **2019**, *745*, 440–449. [CrossRef]
11. Liu, Y.; Xu, H.; Zhu, L.; Wang, X.; Han, Q.; Li, S.; Wang, Y.; Setchi, R.; Wang, D. Investigation into the microstructure and dynamic compressive properties of selective laser melted Ti–6Al–4V alloy with different heating treatments. *Mater. Sci. Eng. A* **2021**, *805*, 140561. [CrossRef]
12. Edwards, P.; Ramulu, M. Fatigue performance evaluation of selective laser melted Ti–6Al–4V. *Mater. Sci. Eng. A* **2014**, *598*, 327–337. [CrossRef]
13. Kasperovich, G.; Hausmann, J. Improvement of fatigue resistance and ductility of TiAl6V4 processed by selective laser melting. *J. Mater. Process. Technol.* **2015**, *220*, 202–214. [CrossRef]
14. Song, Z.M.; Lei, L.M.; Zhang, B.; Huang, X.; Zhang, G.P. Microstructure Dependent Fatigue Cracking Resistance of Ti–6.5Al–3.5Mo–1.5Zr–0.3Si Alloy. *J. Mater. Sci. Technol.* **2012**, *28*, 614–621. [CrossRef]
15. Leuders, S.; Thöne, M.; Riemer, A.; Niendorf, T.; Tröster, T.; Richard, H.A.; Maier, H.J. On the mechanical behaviour of titanium alloy TiAl6V4 manufactured by selective laser melting: Fatigue resistance and crack growth performance. *Int. J. Fatigue* **2013**, *48*, 300–307. [CrossRef]
16. Chastand, V.; Quaegebeur, P.; Maia, W.; Charkaluk, E. Comparative study of fatigue properties of Ti-6Al-4V specimens built by electron beam melting (EBM) and selective laser melting (SLM). *Mater. Charact.* **2018**, *143*, 76–81. [CrossRef]
17. Sun, W.; Ma, Y.e.; Huang, W.; Zhang, W.; Qian, X. Effects of build direction on tensile and fatigue performance of selective laser melting Ti6Al4V titanium alloy. *Int. J. Fatigue* **2020**, *130*. [CrossRef]
18. Liu, S.; Shin, Y.C. Additive manufacturing of Ti6Al4V alloy: A review. *Mater. Des.* **2019**, *164*, 107552. [CrossRef]
19. Karimi, J.; Antonov, M.; Kollo, L.; Prashanth, K.G. Role of laser remelting and heat treatment in mechanical and tribological properties of selective laser melted Ti6Al4V alloy. *J. Alloys Compd.* **2022**, *897*, 163207. [CrossRef]
20. Teixeira, Ó.; Silva, F.J.G.; Ferreira, L.P.; Atzeni, E. A Review of Heat Treatments on Improving the Quality and Residual Stresses of the Ti–6Al–4V Parts Produced by Additive Manufacturing. *Metals* **2020**, *10*, 1006. [CrossRef]
21. Meng, L.X.; Yang, H.J.; Ben, D.D.; Ji, H.B.; Lian, D.L.; Ren, D.C.; Li, Y.; Bai, T.S.; Cai, Y.S.; Chen, J.; et al. Effects of defects and microstructures on tensile properties of selective laser melted Ti6Al4V alloys fabricated in the optimal process zone. *Mater. Sci. Eng. A* **2022**, *830*, 142294. [CrossRef]
22. Gong, H.; Rafi, K.; Gu, H.; Janaki Ram, G.D.; Starr, T.; Stucker, B. Influence of defects on mechanical properties of Ti–6Al–4V components produced by selective laser melting and electron beam melting. *Mater. Des.* **2015**, *86*, 545–554. [CrossRef]
23. Miao, X.; Wu, M.; Han, J.; Li, H.; Ye, X. Effect of Laser Rescanning on the Characteristics and Residual Stress of Selective Laser Melted Titanium Ti6Al4V Alloy. *Materials* **2020**, *13*, 3940. [CrossRef] [PubMed]
24. Xiao, Z.; Chen, C.; Hu, Z.; Zhu, H.; Zeng, X. Effect of rescanning cycles on the characteristics of selective laser melting of Ti6Al4V. *Opt. Laser Technol.* **2020**, *122*, 105890. [CrossRef]

25. Qiu, C.; Wang, Z.; Aladawi, A.S.; Kindi, M.A.; Hatmi, I.A.; Chen, H.; Chen, L. Influence of Laser Processing Strategy and Remelting on Surface Structure and Porosity Development during Selective Laser Melting of a Metallic Material. *Metall. Mater. Trans. A* **2019**, *50*, 4423–4434. [CrossRef]
26. Duan, W.; Wu, M.; Han, J. Effect of laser rescanning on Ti6Al4V microstructure during selective laser melting. *Proc. Inst. Mech. Eng. Part B J. Eng. Manuf.* **2020**, *235*, 763–771. [CrossRef]
27. Kumar, P.; Ramamurty, U. Microstructural optimization through heat treatment for enhancing the fracture toughness and fatigue crack growth resistance of selective laser melted Ti 6Al 4V alloy. *Acta Mater.* **2019**, *169*, 45–59. [CrossRef]
28. Lütjering, G. Influence of processing on microstructure and mechanical properties of (α+β) titanium alloys. *Mater. Sci. Eng. A* **1998**, *243*, 32–45. [CrossRef]
29. Vrancken, B.; Thijs, L.; Kruth, J.-P.; Van Humbeeck, J. Heat treatment of Ti6Al4V produced by Selective Laser Melting: Microstructure and mechanical properties. *J. Alloys Compd.* **2012**, *541*, 177–185. [CrossRef]
30. Liang, Z.; Sun, Z.; Zhang, W.; Wu, S.; Chang, H. The effect of heat treatment on microstructure evolution and tensile properties of selective laser melted Ti6Al4V alloy. *J. Alloys Compd.* **2019**, *782*, 1041–1048. [CrossRef]
31. Tan, X.; Kok, Y.; Toh, W.Q.; Tan, Y.J.; Descoins, M.; Mangelinck, D.; Tor, S.B.; Leong, K.F.; Chua, C.K. Revealing martensitic transformation and alpha/beta interface evolution in electron beam melting three-dimensional-printed Ti-6Al-4V. *Sci. Rep.* **2016**, *6*, 26039. [CrossRef]
32. Kahlin, M.; Ansell, H.; Moverare, J.J. Fatigue behaviour of notched additive manufactured Ti6Al4V with as-built surfaces. *Int. J. Fatigue* **2017**, *101*, 51–60. [CrossRef]
33. Wu, G.Q.; Shi, C.L.; Sha, W.; Sha, A.X.; Jiang, H.R. Effect of microstructure on the fatigue properties of Ti–6Al–4V titanium alloys. *Mater. Des.* **2013**, *46*, 668–674. [CrossRef]
34. Sangid, M.D. The physics of fatigue crack initiation. *Int. J. Fatigue* **2013**, *57*, 58–72. [CrossRef]
35. Wu, L.; Jiao, Z.; Yu, H. Study on small crack growth behavior of laser powder bed fused Ti6Al4V alloy. *Fatigue Fract. Eng. Mater. Struct.* **2022**. [CrossRef]
36. Xu, Z.W.; Liu, A.; Wang, X.S. The influence of building direction on the fatigue crack propagation behavior of Ti6Al4V alloy produced by selective laser melting. *Mater. Sci. Eng. A* **2019**, *767*, 138409. [CrossRef]
37. Sauer, C.; Lutjering, G. Influence of alpha layers at beta grain boundaries on mechanical properties of Ti-alloys. *Mater. Sci. Eng. A-Struct. Mater. Prop. Microstruct. Process.* **2001**, *319*, 393–397. [CrossRef]
38. Biswal, R.; Syed, A.K.; Zhang, X. Assessment of the effect of isolated porosity defects on the fatigue performance of additive manufactured titanium alloy. *Addit. Manuf.* **2018**, *23*, 433–442. [CrossRef]
39. Mine, Y.; Takashima, K.; Bowen, P. Effect of lamellar spacing on fatigue crack growth behaviour of a TiAl-based aluminide with lamellar microstructure. *Mater. Sci. Eng. A* **2012**, *532*, 13–20. [CrossRef]